Structural, thermal and electrical properties of $Na_{1+x}Al_xTi_{2-x}P_3O_{12}$ (x = 0.3) solid electrolytes

Ademola J. Adetona

adetonaademola077@gmail.com

The University of Sheffield

Ge Wang

University of Manchester

Ayorinde O. Nejo

University of Lagos

Cheryl Shaw

The University of Sheffield

Beatia In Siame

The University of Sheffield

Research Article

Keywords: Na1.3Al0.3Ti1.7(PO4)3, Solid electrolyte, Dilatometry, DSC/TGA, Electrochemical Impedance Spectroscopy

Posted Date: August 29th, 2024

DOI: https://doi.org/10.21203/rs.3.rs-4839121/v1

Additional Declarations: No competing interests reported.

Abstract

Investigation of the commercially available $Na_{1.3}Al_{0.3}Ti_{1.7}(PO_4)_3$ (NATP) solid electrolyte for Na-ion solid-state batteries (SIBs) application requires a comprehensive understanding of its microstructural, thermal behaviour and electrical properties. In this study, we investigated the solid electrolyte properties of NATP through different spectroscopic techniques, including XRD, SEM, DSC/TGA, Dilatometer, and Impedance Spectroscopy. The impact of sintering temperature on the densification, microstructural and electrical properties was investigated. Both Archimedes and geometric density measurement methods were utilised to determine the relative density (ρ_r) of the sintered ceramics. Additionally, we investigated the optimum temperature at which the $AlPO_4$ secondary phase is suppressed/minimised for this solid electrolyte. Refinement of the phases present in the NATP was studied using Topas 5 software to provide insight into the crystalline structure of the ceramic. The ionic conductivity studies of the NATP solid electrolyte were found to be in the range of 10^{-7} – 10^{-8} S/cm at 25°C, and the activation energies were in the range of 0.46 ± 0.35 eV. This study provides a thorough understanding of NATP properties, indicating its potential as a solid electrolyte.

1. Introduction

Solid electrolytes are widely employed in various energy storage technologies, including batteries and fuel cells [1]. Unlike traditional liquid electrolytes, solid electrolytes offer distinct advantages, such as enhanced safety [1], improved stability [2], and a wide operating temperature range [1–3]. Of particular interest are solid electrolytes containing Na^+ ions, which are used in sodium-ion solid-state batteries (SSSBs) [3–5]. Sodium-ion batteries (SIBs) have emerged as a promising alternative to lithium-ion batteries (LIBs), primarily due to the abundance and lower cost of Na-ion compounds. Inorganic ceramics that utilise Na^+-ion are emerging as promising options due to their excellent mechanical and electrochemical stability [6]. Perovskites [3, 7, 8], Argyrodites [9], NASICON [10–12], NASICON-type [3, 13–15] and Garnet materials [3, 16] are among the various types of Na^+-ion ceramic materials studied. The phosphate-based NASICON-type compounds have found widespread usage in numerous applications, making them attractive options in SSSBs [10–15]. Traditional sintering has been the primary route for densifying ceramic materials and ionic conductors [17, 18].

Phosphate-based NASICON-type solid electrolytes are particularly intriguing due to their low electronic conductivity [14, 15, 19], good stability, and compatibility with SSSBs, making them a promising candidate for practical applications [20–22]. Furthermore, phosphate ions have a lattice structure that can accommodate Na^+ ions, facilitating ion transport within the solid electrolyte [23]. However, phosphate-based solid electrolytes have low room temperature ionic conductivity (10^{-5} – 10^{-8} S/cm) [14, 15, 24–27]. $NaTi_2PO_{12}$ (NTP) has been used as a luminescence material [28] in nuclear waste management [29] and SSSBs [30–32]. Several approaches to enhancing the electrochemical properties of NTP have been investigated, including particle size reduction [30], surface modifications [31], and the use of dopants (e.g. Al and Cr). Al^{3+}/Cr^{3+} doping allows more Na-ion to be accommodated in the structure, which compensates for the charge balance and improves the potential for its use as a solid electrolyte [33].

$Na_{1.3}Al_{0.3}Ti_{1.7}(PO_4)_3$ (NATP) has a NASICON-type framework with MO_6 octahedra, PO_4 and TiO_4 occupying the tetrahedra site. It has a rhombohedral structure (*R-3c*) with Na-ions located at two different sites in the *R-3c* structure. The Na1 (Wyckoff position 18e) site is almost empty, and Na2 (Wyckoff position 6b) is fully occupied. Within the 3D structure, Na^+ ions migrate by hopping mechanism from the occupied site (Wyckoff position 6b) to the empty lattice (Wyckoff position 18e). Various studies have investigated the preparation of $Na_{1.3}Al_{0.3}Ti_{1.7}(PO_4)_3$ and studied the properties of these solid electrolytes.

Table 1 explores various preparation methods of phosphate-based solid electrolytes, conditions (the sintering temperatures and times), densities, ionic conductivities, activation energy and reactant modifications adopted to minimise the formation of $AlPO_4$ as a secondary phase.

Table 1
Preparation methods, sintering temperatures, times, relative density, ionic conductivity and activation energy (E_a) of phosphate-based solid electrolytes.

Phosphate-based solid electrolytes	Preparation methods	Sintering Temp. (°C)	Time (Hours)	Density /gcm^{-3}	Ionic conductivity 25°C (S/cm)	E_a (eV)	Ref.
$Na_{1.3}Al_{0.3}Ti_{1.7}(PO_4)_3$	Conventional	900	11	90	2.7×10^{-7}	0.61	26
$Na_{1.3}Al_{0.3}Ti_{1.7}(PO_4)_3$	Fused filament fabrication	1100	12	94.27	1.71×10^{-4} @ 200°C	0.58	14
$Na_{1.3}Al_{0.4}Ti_{1.6}(PO_4)_3$	Conventional	725	24	-	5.6×10^{-8}	0.54	15
$Na_3Ti_2(PO_4)_3$	Melt quenching	827	5	-	3.22×10^{-5}	0.531	32
$Na_{3.25}Cr_{0.25}Ti_{1.75}(PO_4)_3$	Melt quenching	827	5	-	7.42×10^{-5}	0.512	32
$Na_{3.5}Cr_{0.5}Ti_{1.5}(PO_4)_3$	Melt quenching	827	5	-	2.12×10^{-4}	0.486	32
$Na_{3.75}Cr_{0.75}Ti_{1.25}(PO_4)_3$	Melt quenching	827	5	-	5.38×10^{-5}	0.521	32
$Li_{1.3}Al_{0.3}Ti_{1.7}(PO_4)_3$	Spark Plasma Sintering	900	12	96.7	1.0×10^{-4}	-	24
$Li_{1.3}Al_{0.3}Ti_{1.7}(PO_4)_3$	Spark Plasma Sintering	950	12	96	9.4×10^{-5}	-	24
$Li_{1.3}Al_{0.3}Ti_{1.7}(PO_4)_3$	Spark Plasma Sintering	1000	12	95.9	1.2×10^{-4}	-	24
$Li_{1.3}Al_{0.3}Ti_{1.7}(PO_4)_3$	Spark Plasma Sintering	1050	12	93.2	5.5×10^{-5}	-	24
$Li_{1.3}Al_{0.3}Ti_{1.7}(PO_4)_3$	Conventional	900	10	-	5.06×10^{-7}	0.32	25

In this work, we have conventionally sintered $Na_{1.3}Al_{0.3}Ti_{1.7}(PO_4)_3$ (NATP) to identify the optimum sintering temperatures at which the $AlPO_4$ secondary phase is suppressed and improved the thermal behaviour, phase, morphology, and its ionic conductivity compared with reports in the scientific literature.

2. Experimental methods

2.1 Ceramic fabrication: NATP powder was sourced from the NEI Corporation and used without further processing. The NATP pellets were conventionally sintered between 850 – 1000 °C in air for 6 - 12 hours.

2.2 Structural and microstructural characterisation: The size distribution of the NATP green powder was measured using the Malvern Mastersizer Particle Analyser 3000 in a hydro-dispersion mode. The volume changes as a function of temperature were studied using a Netzsch LFA hyper flash high-temperature Dilatometer, and the density of the sintered NATP pellets was measured using Archimedes' and geometric methods. Thermogravimetry analysis (TGA) and Differential Scanning Calorimetry (DSC) measurements were performed using the SDT Q600 model to study the thermal behaviour of the ceramic. A PANalytical Aeris X-ray diffractometer with Cu-Kα radiation (λ= 0.154 nm) in the 2θ range 10 – 60°, with a step size of 0.02°, was used to study the diffraction data of the NATP. Phase refinement was carried out on the diffraction data of the NATP ceramics using Topas 5 software. Microstructural studies were performed on the sintered pellet surfaces using an FEI Inspect F50 Scanning electron microscopy.

2.3 Impedance spectroscopy: Impedance measurement was performed on the lightly ground surface of the sintered NATP pellets with Au paste alloy, fired at 850 °C for 2 hours. Electrochemical Impedance spectroscopy (EIS) was performed using an Agilent 4294A from RT to 800 °C at intervals of 50 °C. The Agilent 4294A was calibrated using a blank, open, and closed circuit to correct errors associated with the measurement. After the impedance (Z*) measurement, a geometric correction factor accounting for the pellet thickness and sample-electrode area (surface area normalisation) was applied to the data. Data analysis and circuit fitting were performed using ZVIEW-impedance Software version 2.4 Scribner Associates.

3. Results

3.1. Particle Size Distribution

The size distribution of the NATP green powder is shown in Fig. 1. Prior to the measurement, the refractive index of the dispersant (H_2O) and the NATP green powder was selected to be approximately 1.33 and 1.72, respectively. To ensure accurate and reliable size distribution, ten different measurements were taken, and the average was recorded. The size distribution of the NATP green powder was recorded at various D_x values (D_{10}, D_{50} and D_{90}). The D_x refer to the diameter of the grain at a certain percentile point in the size distribution curve, and the number in parentheses represents the percentile point. The NATP green powder shows a bimodal size distribution, suggesting the grains are irregular and agglomerated. The size distribution of the NATP is similar to that reported by [24]. Table S1 shows the average size distribution at different D_x values of NATP. D_{10} refers to the diameter at which 10% of the grains in the sample are smaller than the average grain size. D_{50} represents the median diameter at which 50% of the grains in the sample are smaller than the average grain size, and D_{90} indicates the diameter below which 90% of the grains in the sample are smaller than the average grain size. It should be noted that the Mastersizer only provides an estimated size distribution and not the powder's grain size.

3.2 Dilatometry

The changes in the volume of the NATP green pellets as a function of temperature are shown in Fig. 2. NATP green powder was first pressed into 12–15 mm long cylindrical pellets using a cold isostatic press, and the change in length ($\triangle L/L_o$) of the NATP cylindrical pellets as a function of the temperature (°C) was recorded over a wide temperature range between room temperature and 1100°C. A small change in the pellet length ($\triangle L \approx 0.005$ m) was recorded between room temperature and 878°C, and a further drop in the ceramic length ($\triangle L \approx 0.055$ m) was recorded between 878 and 1050°C, as shown in Fig. 2, similar to what was obtained for LATP by [24]. Investigation into the melt pool phase of NATP, as observed in NZSP [10], resulted in a burnt ceramic, indicating there are no such phases present in the NATP ceramic. In addition, the volume contraction as a function of temperature predicts the optimum sintering temperature of the NATP ceramic. Based on the dilatometer data, the optimum sintering temperature range for NATP is between 850–1000°C.

3.3 Thermogravimetry Analysis

Thermogravimetry analysis (TGA) studies of the NATP ceramic reveal the sample's thermal behaviour. An overall weight loss of 0.14 mg (≈ 2.0%) was recorded throughout the temperature range of 0 to 1100°C, Fig. 3 (black triangle). This weight loss indicates that the sample underwent thermal decomposition and/or released a volatile element. As the temperatures increased, subsequent drops in sample weight were observed. A significant drop in sample weight of 0.05 mg (≈ 0.6%) was observed at a range of 88 to 162°C. This pronounced weight loss could be attributed to the volatilisation of lighter elements such as Na^+ ions. As the sintering temperature increases, a further weight drop of 0.03 mg (≈ 0.5%) was observed between 600 and 900°C. This weight loss suggests the onset of another decomposition or release of volatile species such as $AlPO_4$. The weight variations observed in TGA indicate the different processes occurring during sintering. A similar trend was observed for LATP [24, 25]. Further analysis and investigation are required to identify the specific elements or compounds responsible for the weight loss observed at different temperature ranges. Figure S1 provides a supporting image of the thermal behaviour (TGA) of the NATP.

3.4 Differential Scanning Calorimetry.

Distinct heat flows were observed during the Differential Scanning Calorimetry (DSC) analysis of the NATP, indicating various thermal changes within the Na-ion compound. Two significant heat flows were observed at 257°C and 865°C, respectively, Fig. 3 (red circle). At 257°C, a less pronounced heat flow was recorded, indicating a smaller energy exchange associated with a structural or phase change (crystallization temperature) in the NATP. This heat flow suggests a subtle rearrangement of the NATP lattice structure. At 865°C, a high heat flow of (≈ 8.57 J/g) was observed, indicating a significant energy exchange (glass transition) within the NATP. The pronounced heat flow at 865°C corresponds to a temperature point where a more substantial rearrangement (glass transition) of the NATP's lattice structure occurs. A similar observation was reported by [26]. The exothermic change in the heat flow indicates that a higher energy is

required to overcome the forces holding the NATP constituents together. Figure S2 provides a supporting figure of the thermal behaviour of the NATP.

3.5 X-ray Diffraction

Figures 4 and 5 show the XRD patterns of the NATP powder and sintered ceramics. The diffraction peaks were matched to a rhombohedral $Na_{1.3}Al_{0.3}Ti_{1.7}(PO_4)_3$ with space group R-3c and PDF No 01-014-7800 (Fig. 4a). An unknown secondary peak is observed at 22.4, 2θ° for the NATP green powder (Fig. 4b and 5a). The XRD patterns of the conventional sintered NATP ceramics at different sintering temperatures and times are shown in Figs. 4c and 5(b-e). Prior to sintering, the NATP pellets were buried in NATP green powder and sintered between 850–1000°C for 6–12 hours to investigate the optimum sintering temperature, suppress the formation of $AlPO_4$ secondary phase, improve densification and optimise ionic conductivity. The X-ray diffraction patterns of the NATP pellets sintered conventionally at 850, 900, 950 and 1000°C were matched against the diffraction pattern of the $Na_{1.3}Al_{0.3}Ti_{1.7}P_3O_{12}$ green powder. All the XRD patterns of the sintered NATP ceramics have an impurity phase of $AlPO_4$ peaks (x-symbol) at 21.8, 2θ°, similar to the literature [14–16, 24, 25, 33]. However, the $AlPO_4$ impurities phase was minimal at 900°C for 12 hours, Fig. 4c which also had the highest geometric relative density (section 3.7). In addition, the unknown peak present in the NATP green powder at 22.4, 2θ° was absent at this temperature (900°C for 12 hr). Decreasing the sintering temperature to 850°C for 12 hours, Fig. 5b and decreasing the sintering time to 6 hours at 900°C, Fig. 5c also eliminated the unknown secondary peaks but did not minimise the $AlPO_4$ impurity phase and sintering at this condition resulted in a fragile ceramic with poor relative density (section 3.7). Increasing the sintering temperature to 950°C for 12 hours, Fig. 5d and 1000°C for 12 hr, Fig. 5e, increased the volume fraction of the $AlPO_4$ impurity phase at 21.8, 2θ° and further re-introduced the unknown peak at 22.4, 2θ°. All efforts to suppress completely the $AlPO_4$ impurity phase were unsuccessful consistent with previous reports [14, 16, 24, 25].

3.6 Rietveld refinement

Diffraction data of the conventionally sintered NATP at different temperatures and times were analysed using a full-pattern Rietveld refinement method to investigate the crystal structure and phase formation of NATP. The refined data confirmed two phases, *R-3c* NATP and *F1* $AlPO_4$, at all sintered temperatures and times, Table 2. The percentage composition of the $AlPO_4$ (≈ 4.5%) impurity phase was minimal at 900°C for 12 hours compared to NATP sintered at other temperatures and times. In fact, NATP sintered at 950°C for 12 hours has the highest $AlPO_4$ impurity phase (≈ 27.0%). The fitting of the $AlPO_4$ impurity phase and the NATP phase are shown in the zoom-in plot, Fig. 6 (a-e), and the diffraction data of NATP sintered at 900°C for 12 hours are similar to the reported data [15, 33], Fig. 6f. The lattice parameters, theoretical density, goodness of fit (GoF), unit cell volume and the percentage composition of the two phases observed are shown in Table 2.

Table 2
Refined parameters, phase fractions, the goodness of fit (GoF), cell volume and theoretical density of $Na_{1.3}Al_{0.3}Ti_{1.7}(PO_4)_3$ ceramic sintered at different temperatures and time.

NATP	Phase fraction (%)		Lattice parameters (Å)		GoF	Unit cell volume	Theoretical density
Sintered Temp	*R-3c* NATP	*F1-* $AlPO_4$	a	c			
850°C / 12hr	89.0	11.0	8.469	21.812	1.93	1354.72	2.966
900°C / 6hr	92.0	8.0	8.484	21.769	1.48	1356.90	2.961
900°C / 12hr	95.5	4.5	8.479	21.775	1.93	1355.70	2.964
950°C / 12hr	72.5	27.5	8.473	21.829	3.24	1357.00	2.961
1000°C / 12hr	79.0	21.0	8.475	21.786	3.55	1355.00	2.965

3.7. Relative density

The experimental density of NATP sintered pellets was measured using Archimedes and geometric methods, and the results were compared with the theoretical density of NATP obtained from the refinement data and the literature [15]. The relative density (ρ_r) of NATP was calculated from its theoretical densities of 2.96 g/cm^3, Table 2. Figure 7 shows the relative density of NATP sintered at different temperatures for 12 hours using Archimedes (blue circle) and geometric (red star) methods. The ρ_r follows similar trends to the literature [25, 26]. The ρ_r of the NATP ceramic sintered at 900°C for 12 hours is comparable to [26] using the geometric technique.

3.8 Scanning electron microscopy

Figure 8 (a-e) shows the SEM micrographs of the sintered NATP ceramics surfaces at different temperatures. At 850°C for 12 hours, Fig. 8a, loosely bonded particles and pores are evident. Conversely, at 950°C for 12 hours, Fig. 8d, larger grain sizes and increased agglomeration are observed. Samples sintered at 900°C for 12 hours show fewer loosely bonded grains compared to others. In general, sintering conditions significantly affect NATP ceramic morphology and microstructure, with optimal conditions leading to reduced loosely bonded grains and enhanced densification, consistent with the literature [25, 32, 33].

3.9 Impedance Spectroscopy

Figure 9 (a - f) shows the Complex Impedance Plane, Z* plots at 25°C for $Na_{1.3}Al_{0.3}Ti_{1.7}(PO_4)_3$ ceramics that were sintered at different temperatures (850–1000°C). At 25°C, all the sintered ceramics show a

single, well-resolved arc with a high-frequency zero intercept on the Z' axis. The Z* data in Fig. 9 (a - f) were modelled by using an equivalent circuit that is based on a single resistor connected in series with a parallel Resistor-Capacitor element. The single resistor (associated with the high frequency zero intercept of the Z' axis) is attributed to the total resistivity of the ceramic (R_T). The total (dc) resistivity estimated from the arc ranges from 6.0 x 10^6 Ωcm to 1.1 x 10^7 Ωcm, which is consistent with the literature [16, 24–25, 33]. The capacitance, total resistance, relaxation frequency, and total conductivity at 25°C are shown in Table 3. The capacitance values are in the range of picoFarad/cm, and the relaxation frequencies (RF) of all sintered NATP ceramics are within the range of 10^{-4} Hz, as shown in Fig. 9 (a-e). Figure 9f presents a comparison of the Z* plots for $Na_{1.3}Al_{0.3}Ti_{1.7}(PO_4)_3$ ceramics in the complex impedance plane at 25°C. Notably, the sample sintered for 12 hours at 900°C exhibits the highest conductivity, measuring 2.45 x 10^{-7} S/cm at 25°C. However, the ionic conductivities of other NATP ceramics sintered between 850–1000°C are within the margin.

Figure 10 shows the Arrhenius plots of the total conductivity ($\sigma_t = 1/R_t$) of the NATP solid electrolyte. The activation energies associated with each sintering temperature were calculated and recorded. The activation energy (E_a) observed in our study is comparatively lower, albeit comparable to the literature [33].

Table 3
Room temperature total Capacitance, Resistance, Relaxation frequency and total ionic conductivities of $Na_{1.3}Al_{0.3}Ti_{1.7}PO_{12}$ solid electrolyte at different sintering temperatures and times.

NATP at 25°C		**Capacitance (F/cm)**	**Resistance (Ω)**	**Relaxation frequency (Hz)**	**Conductivity (S/cm)**
Temp (°C)	Time (hr)	$C_T = 1/2\pi fmaxR$	R_T	R_F	σ_T / 25°C
850	12	7.114 x 10^{-13}	1.073 x 10^7	1.0 x 10^4	9.32 x 10^{-8}
900	6	9.946 x 10^{-13}	5.891 x 10^6	2.0 x 10^4	1.69 x 10^{-7}
900	12	1.874 x 10^{-12}	4.090 x 10^6	1.5 x 10^4	2.45 x 10^{-7}
950	12	1.731 x 10^{-12}	1.123 x 10^7	1.0 x 10^4	8.90 x 10^{-8}
1000	12	1.876 x 10^{-12}	6.773 x 10^6	1.0 x 10^4	1.48 x 10^{-7}

4. Conclusions

We have investigated the solid electrolyte $Na_{1.3}Al_{0.3}Ti_{1.7}(PO_4)_3$ (NATP) using XRD, SEM, DSC, TGA, dilatometry and Impedance spectroscopy. Our results reveal that the optimal sintering conditions are at 900°C for 12 hours. These conditions minimise the presence of the $AlPO_4$ secondary phase, leading to improved density and ionic conductivity. DSC identifies significant heat flows indicating energy exchange within the NATP's structure, while TGA shows weight loss due to thermal decomposition/volatilization during sintering. Sintering conditions significantly influence NATP ceramic morphology and

microstructure. The highest ionic conductivity obtained at 25°C for the solid electrolyte was 2.45 x 10^{-7} S/cm at the optimal sintering temperature, which was similar to the literature. The activation energy (E_a) observed in our study is comparatively low, albeit similar to previous works.

Declarations

Declaration and Conflict of Interest

The authors declare that they have no known competing financial interests that could have influenced the work reported in this paper.

Author Contribution

Ademola AdetonaConceptualization: The primary ideas and research question were conceived by the author.Methodology: The author developed the research design and collected and analyzed the data.Investigation: The author conducted experiments and gathered relevant data.Writing - Original Draft: The author wrote the initial draft of the manuscript.Writing - Review & Editing: The author contributed to the revision and editing process.Visualization: The author created the figures and visual elements used in the manuscript.Validation: The author verified the accuracy and integrity of the research findings.Funding Acquisition: The author secured financial support for the project.Project Administration: The author managed the project and ensured its smooth execution.Supervision: The author supervised and coordinated the overall research project.Ge Wang Methodology: The author collected and analyzed the data.Funding Acquisition: The author secured financial support for the project.Writing - Review & Editing: The author contributed to the revision and editing process.Visualization: The author created the figures and visual elements used in the manuscript.Validation: The author verified the accuracy and integrity of the research findings.Ayorinde NejoWriting - Review & Editing: The author provided critical feedback and contributed to the improvement of the manuscript.Validation: The author verified the accuracy and integrity of the research findings.Cheryl ShawMethodology: The author analyzed the SEM data.Beatia In SiameMethodology: The author collected some of the data.

Acknowledgement

The authors acknowledge the support of: The Tertiary Education Trust Fund of Nigeria (TETFUND)The Functional Materials and Devices group of the Department of Material Science and Engineering, the University of Sheffield, United Kingdom.The Dame Kathleen Ollerenshaw Fellowship provided by the University of Manchester.

References

1. S. Chen, K. Wen, J. Fan, Y. Bando, D. Golberg, Progress and future prospects of high-voltage and high-safety electrolytes in advanced lithium batteries: from liquid to solid electrolytes, Journal of Materials

Chemistry. A, Materials for Energy and Sustainability. 6 (2018) 11631–11663. https://doi.org/10.1039/c8ta03358g.

2. R. Chen, Q. Li, X. Yu, L. Chen, H. Li, Approaching Practically Accessible Solid-State Batteries: Stability Issues Related to Solid Electrolytes and Interfaces, Chemical Reviews. 120 (2019). https://doi.org/10.1021/acs.chemrev.9b00268.
3. Z. Wu, Z. Xie, A. Yoshida, Z. Wang, X. Hao, A. Abudula, G. Guan, Utmost limits of various solid electrolytes in all-solid-state lithium batteries: A critical review, Renewable and Sustainable Energy Reviews. 109 (2019) 367–385. doi.org/10.1016/j.rser.2019.04.035.
4. E.A. Wu, S. Banerjee, H. Tang, P.M. Richardson, Jean-Marie Doux, J. Qi, Z. Zhu, A. Grenier, Y. Li, E. Zhao, G. Deysher, E. Sebti, H. Nguyen, R.M. Stephens, G. Verbist, K.W. Chapman, R.J. Clément, A. Banerjee, Ying Shirley Meng, Shyue Ping Ong, A stable cathode-solid electrolyte composite for high-voltage, long-cycle-life solid-state sodium-ion batteries, Nature Communications. 12 (2021). https://doi.org/10.1038/s41467-021-21488-7.
5. Z. Zhang, S. Wenzel, Y. Zhu, J. Sann, S. Lin, J. Yang, X. Yao, Y. Hu, C. Wolverton, H. Li, L. Chen, J. Janek, $Na_3Zr_2Si_2PO_{12}$: A Stable Na+-Ion Solid Electrolyte for Solid-State Batteries, ACS Applied Energy Materials. 3 (2020) 7427–7437. doi.org/10.1021/acsaem.0c00820.
6. S. Gandi, V.S. Chidambara Swamy Vaddadi, S.S. Sripada Panda, N.K. Goona, S.R. Parne, M. Lakavat, A. Bhaumik, Recent progress in the development of glass and glass-ceramic cathode/solid electrolyte materials for next-generation high capacity all-solid-state sodium-ion batteries: A review, Journal of Power Sources. 521 (2022) 230930. https://doi.org/10.1016/j.jpowsour.2021.230930.
7. E. Aydın, T.G. Allen, M. De Bastiani, A. Razzaq, L. Xu, E. Ugur, J. Liu, S. De Wolf, Pathways toward commercial perovskite/silicon tandem photovoltaics, Science. 383 (2024). https://doi.org/10.1126/science.adh3849.
8. I. López-Fernández, D. Valli, C. Wang, S. Samanta, T. Okamoto, Y. Huang, K. Sun, Y. Liu, V.S. Chirvony, A. Patra, J. Zito, Luca De Trizio, D. Gaur, H. Sun, Z. Xia, X. Li, H. Zeng, Iván Mora-Seró, N. Pradhan, J.P. Martínez-Pastor, Lead-Free Halide Perovskite Materials and Optoelectronic Devices: Progress and Prospective, Advanced Functional Materials. (2023). https://doi.org/10.1002/adfm.202307896.
9. H. Kim, Jae Yup Jung, K. Kim, C. Hwang, J. Yu, M. Park, W. Cho, Functionalized Electrode Additive for Simultaneously Reinforcing Chemo-Mechanical Properties of Millimeter-Thick Dry-Electrode for High-Energy All-Solid-State Batteries, Advanced Energy Materials. (2023). https://doi.org/10.1002/aenm.202303965.
10. A.J. Adetona, G. Wang, B. Walkley, D.C. Sinclair, I.M. Reaney, Effect of ZrO_2 stoichiometry on the structural and electrical properties of $Na_3Zr_{2-x}Si_2PO_{12-2x}$ solid electrolyte, Journal of the European Ceramic Society. (2023). doi.org/10.1016/j.jeurceramsoc.2023.12.071.
11. J. Wolfenstine, W. Go, Y. Kim, J. Sakamoto, Mechanical properties of NASICON: A brief review, Ionics. (2022). https://doi.org/10.1007/s11581-022-04820-z.
12. J. Wang, T. He, X. Yang, Z. Cai, Y. Wang, V. Lacivita, H. Kim, B. Ouyang, G. Ceder, Design principles for NASICON super-ionic conductors, Nature Communications. 14 (2023). https://doi.org/10.1038/s41467-023-40669-0.

13. Q. Zhang, M. Jiang, H. Kungl, R.-A. Eichel, Stabilization the Interface of NASICON-type Solid Electrolyte and Li metal by Al Interlayer, Electrochimica Acta. (2024) 143791–143791. https://doi.org/10.1016/j.electacta.2024.143791.
14. A. Candoğan Kutlu, D. Nötzel, C. Ziebert, H. Jürgen Seifert, I. Ul Mohsin, 3D Printing of $Na_{1.3}Al_{0.3}Ti_{1.7}(PO_4)_3$ Solid Electrolyte via Fused Filament Fabrication for All-Solid-State Sodium-ion Batteries, Batteries & Supercaps. (2023). doi.org/10.1002/batt.202300357.
15. F.E. Mouahid, M. Bettach, M. Zahir, P. Maldonado-Manso, S. Bruque, E.R. Losilla, M.A.G. Aranda, Crystal chemistry and ion conductivity of the $Na_{1+x}Ti_{2-x}Al_x(PO_4)_3$ ($0 \leq x \leq 0.9$) NASICON series, Journal of Materials Chemistry. 10 (2000) 2748–2757 https://doi.org/10.1039/b004837m.
16. C. Yang, X. Zhang, J. Kang, C. Wei, P. Sang, S. Lin, B. Sun, J. Fan, B. Jiang, Y. Li, X. Chen, J. Xu, H. Chen, L. Zhang, Recent progress on garnet phosphor ceramics for high power solid-state lighting, Journal of Materials Science & Technology. 166 (2023) 1–20. https://doi.org/10.1016/j.jmst.2023.04.038.
17. R. Chaim, M. Levin, Amit Shlayer, C. Estournès, Sintering and densification of nanocrystalline ceramic oxide powders: a review, 107 (2008) 159–169. https://doi.org/10.1179/174367508x297812.
18. K. Uchino, Manufacturing Methods for Piezoelectric Ceramic Materials, Advanced Piezoelectric Materials. (2017) 385–421. https://doi.org/10.1016/b978-0-08-102135-4.00010-2.
19. S. El Aggadi, M. Ennouhi, A. Boutakiout, A. El Hourch, Progress towards efficient phosphate-based materials for sodium-ion batteries in electrochemical energy storage, Ionics. (2023). https://doi.org/10.1007/s11581-023-04936-w.
20. C. Cao, Y. Zhong, Z. Shao, Electrolyte Engineering for Safer Lithium-ion Batteries: A Review, Chinese Journal of Chemistry. 41 (2023) 1119–1141. https://doi.org/10.1002/cjoc.202200588.
21. C. Luo, M. Yi, Z. Cao, W. Hui, Y. Wang, Review of Ionic Conductivity Properties of NASICON Type Inorganic Solid Electrolyte LATP, ACS Applied Electronic Materials. (2024). https://doi.org/10.1021/acsaelm.3c01747.
22. Y. Yuan, Q. Wei, S. Yang, X. Zhang, M. Jia, J. Yuan, X. Yan, Towards high-performance phosphate-based polyanion-type materials for sodium-ion batteries, Energy Storage Materials. 50 (2022) 760–782. https://doi.org/10.1016/j.ensm.2022.06.008.
23. L. Zhu, Y. Wang, J. Chen, W. Li, T. Wang, J. Wu, S. Han, Y. Xia, Y. Wu, M. Wu, F. Wang, Y. Zheng, L. Peng, J. Liu, L. Chen, W. Tang, enhancing ionic conductivity in solid electrolyte by relocating diffusion ions to under-coordination sites, Science Advances. 8 (2022). https://doi.org/10.1126/sciadv.abj7698.
24. Katja Waetzig, A. Rost, U. Langklotz, B. Matthey, Jochen Schilm, An explanation of the microcrack formation in $Li_{1.3}Al_{0.3}Ti_{1.7}(PO_4)_3$ ceramics, Journal of the European Ceramic Society. 36 (2016) 1995–2001. https://doi.org/10.1016/j.jeurceramsoc.2016.02.042.
25. K. Kwatek, J.L. Nowiński, Electrical properties of $LiTi_2(PO_4)_3$ and $Li_{1.3}Al_{0.3}Ti_{1.7}(PO_4)_3$ solid electrolytes containing ionic liquid, Solid State Ionics. 302 (2017) 54–60. https://doi.org/10.1016/j.ssi.2016.11.020.
26. M. Rohde, I.U.I. Mohsin, C. Ziebert, H.J. Seifert, Ionic and Thermal Transport in Na-Ion-Conducting Ceramic Electrolytes, International Journal of Thermophysics. 42 (2021).

https://doi.org/10.1007/s10765-021-02886-x.

27. Y. Li, Z. Ding, K. Wang, L. Wan, T. Lu, G. Zhu, Z. Gong, L. Pan, Suppressing the oxygen-related parasitic reactions in $NaTi_2(PO_4)_3$-based hybrid capacitive deionisation with cation exchange membrane, Journal of Colloid and Interface Science. 591 (2021) 139–147. https://doi.org/10.1016/j.jcis.2021.02.013.
28. R.S. Boyko, O.V. Chukova, O.V. Gomenyuk, P.G. Nagornyi, S.G. Nedilko, Origin of red luminescence of sodium titanium phosphate crystals, Physica Status Solidi (C). 2 (2005) 712–715. https://doi.org/10.1002/pssc.200460272.
29. R. Raja Madhavan, A.S. Gandhi, K.V. Govindan Kutty, Sodium titanium phosphate $NaTi_2(PO_4)_3$ waste forms for immobilisation of simulated high-level waste from fast reactors, Ceramics International. 43 (2017) 9522–9530. https://doi.org/10.1016/j.ceramint.2017.04.138.
30. H. Dai, W. Xu, Z. Hu, Y. Chen, J. Gu, F. Xie, W. Wei, R. Guo, G. Zhang, Novel Solid-State Sodium-ion Battery with Wide Band Gap $NaTi_2(PO_4)_3$ Nanocrystal Electrolyte, ACS Omega. 6 (2021) 11537–11544. https://doi.org/10.1021/acsomega.1c00664.
31. M. Wu, W. Ni, J. Hu, J. Ma, NASICON-Structured $NaTi_2(PO_4)_3$ for Sustainable Energy Storage, Nano-Micro Letters. 11 (2019). https://doi.org/10.1007/s40820-019-0273-1.
32. S. Sundar Gandi, Suman Gandi, Naresh Kumar Katari, Wanichaya Mekprasart, Wisanu Pecharapa, D.P. Dutta, Balaji Rao Ravuri, Improvement in fast Na-ion conduction in $Na_{3+x}Cr_xTi_{2-x}(PO_4)_3$ glass–ceramic electrolyte material for Na-ion batteries, Journal of the Iranian Chemical Society. 17 (2020) 2637–2649. https://doi.org/10.1007/s13738-020-01960-9.
33. A.M. Nieto-Muñoz, J.F. Ortiz-Mosquera, Ana C.M. Rodrigues, The role of Al^{3+} on the microstructural and electrical properties of $Na_{1+x}Al_xTi_{2-x}(PO_4)_3$ NASICON glass-ceramics, Journal of Alloys and Compounds. 820 (2020) 153148–153148. https://doi.org/10.1016/j.jallcom.2019.153148.

Figures

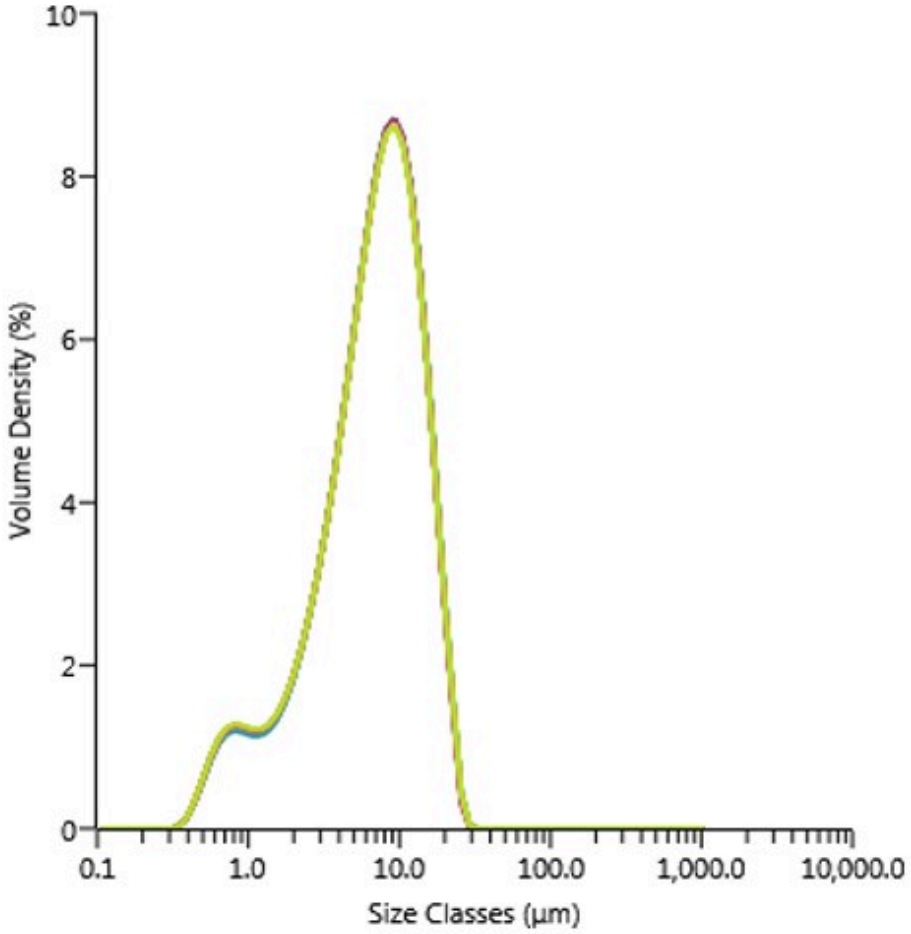

Figure 1

Particle size distribution of NATP green powder.

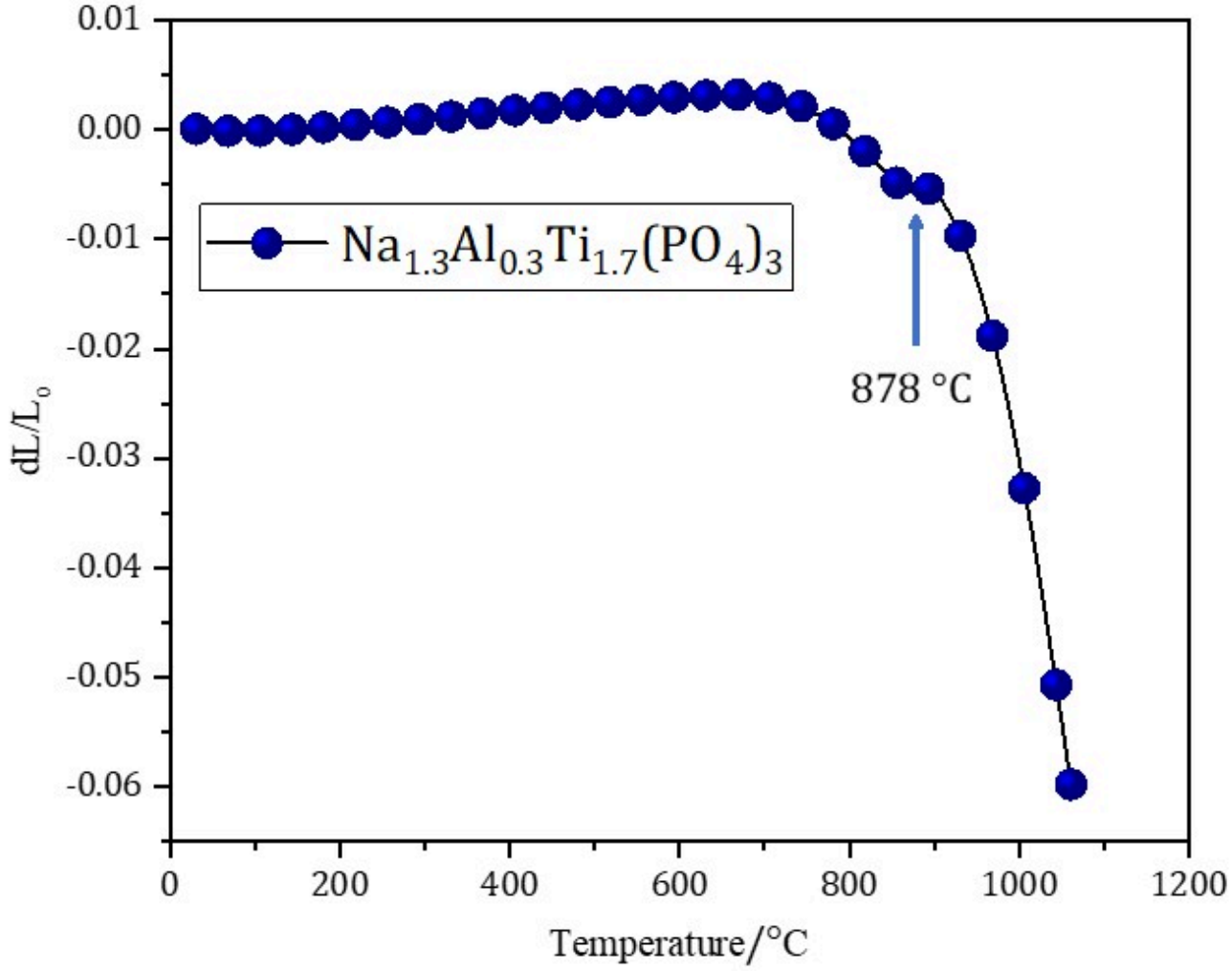

Figure 2

Volume contraction as a function of Temperature plot of $Na_{1.3}Al_{0.3}Ti_{1.7}P_3O_{12}$ using a Dilatometer.

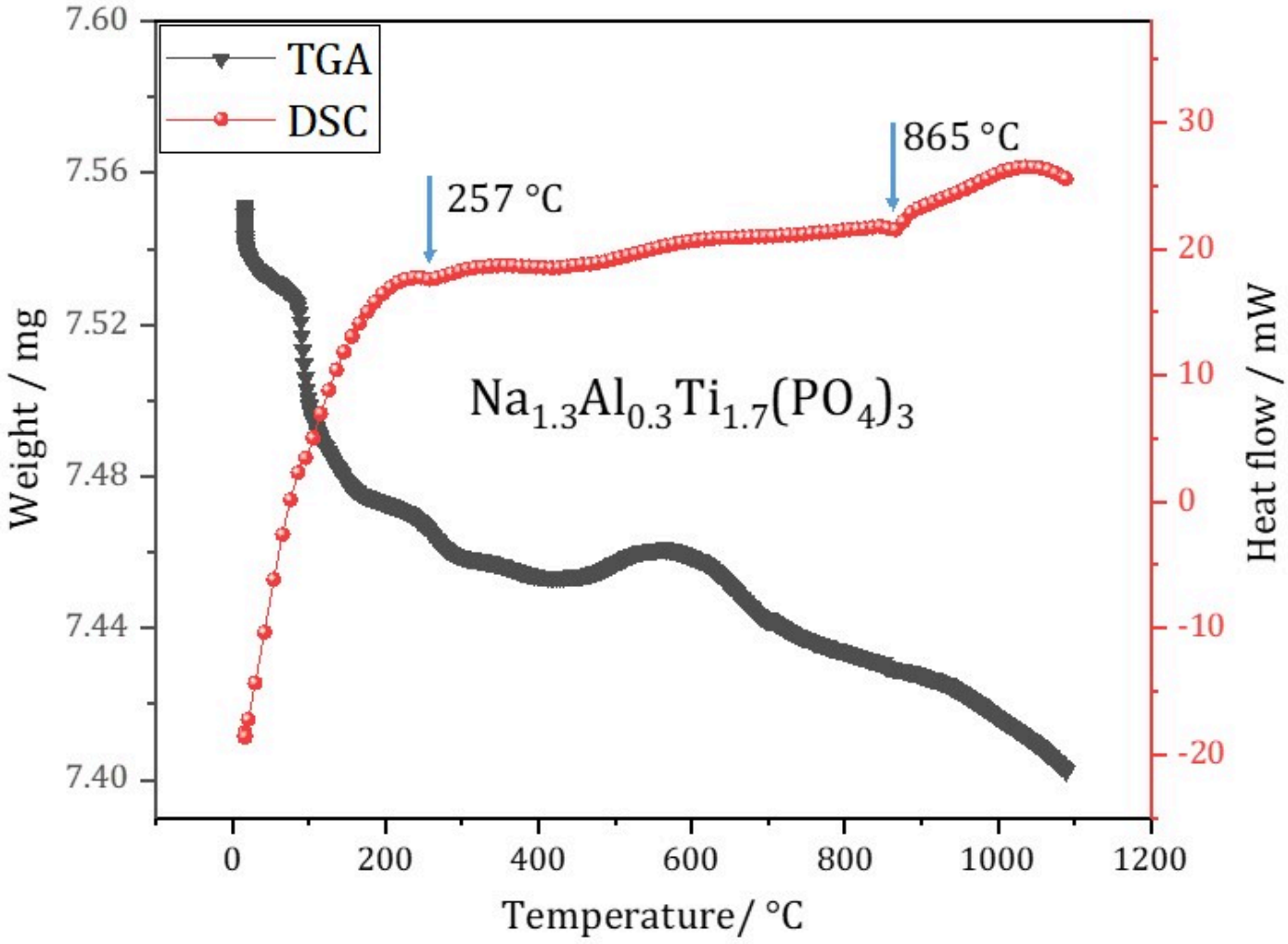

Figure 3

Thermogravimetry Analysis (TGA, black) and Differential Scanning Calorimetry (DSC, red) plots of $Na_{1.3}Al_{0.3}Ti_{1.7}(PO_4)_3$ as a function of Temperature.

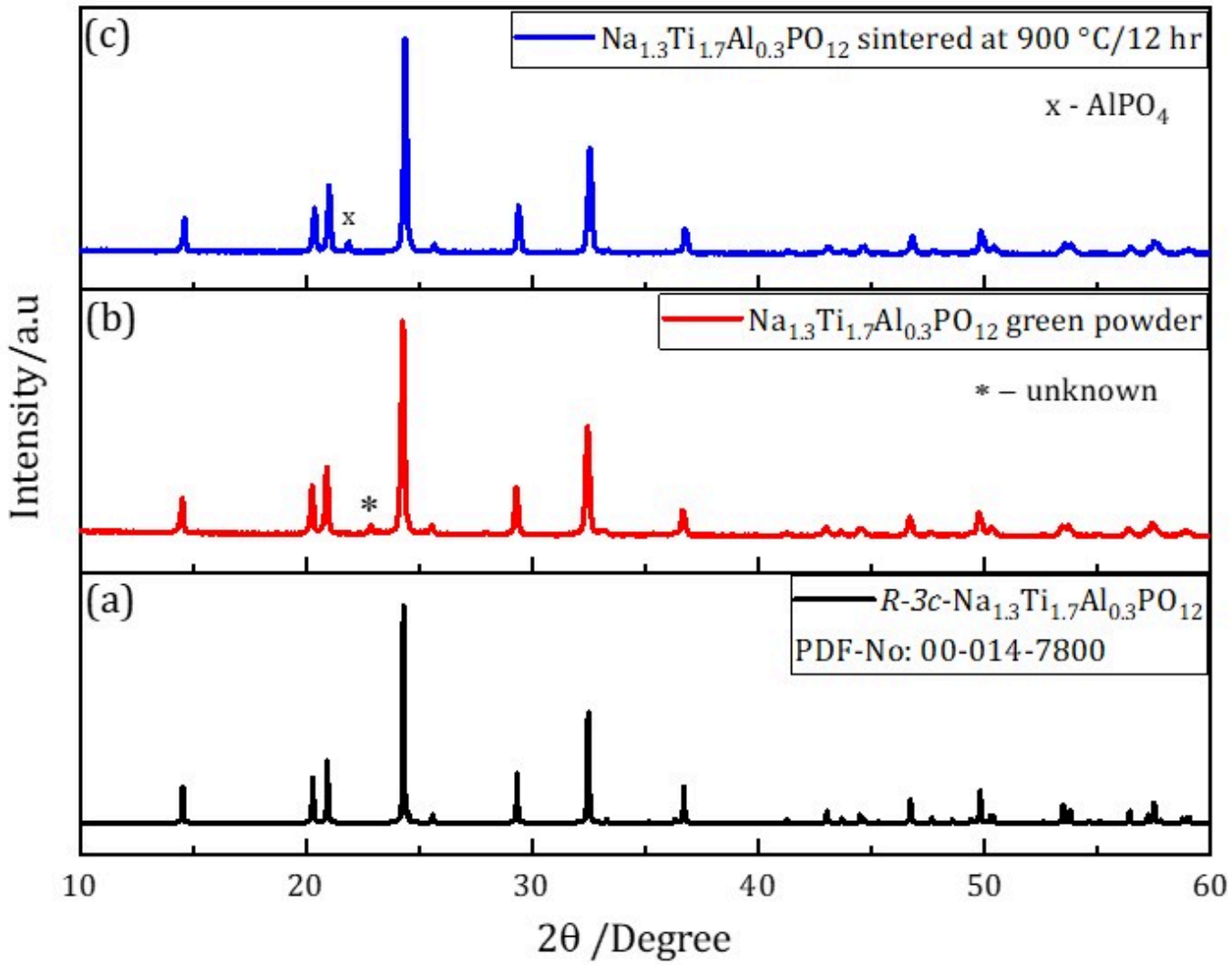

Figure 4

Room temperature X-ray diffraction patterns of NATP green powder and NATP sintered pellets at 900 °C/12 hours matched against *R-3c* NATP with PDF No: 00-014-7800.

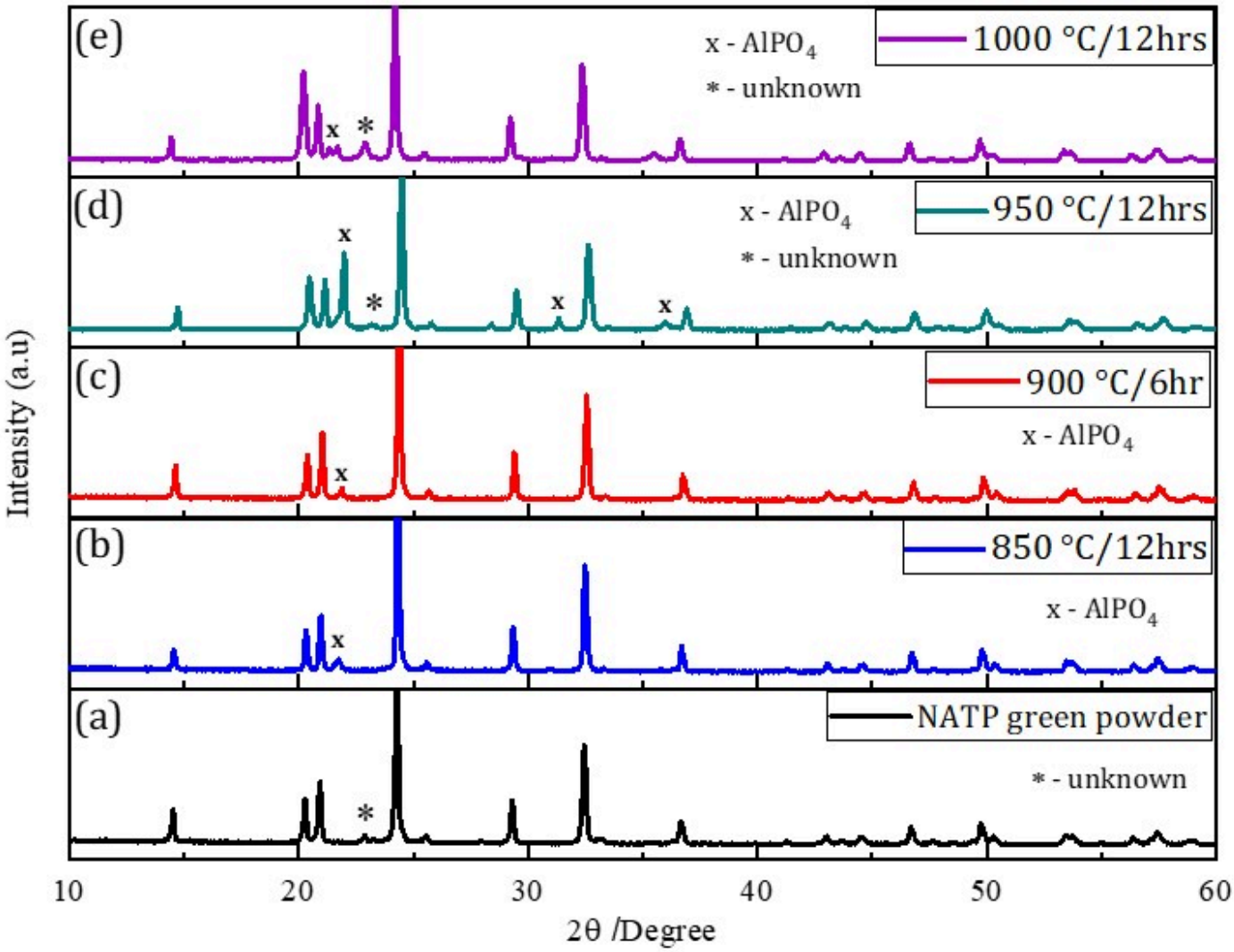

Figure 5

Room temperature X-ray diffraction patterns of NATP powder and conventional sintered NATP at different temperatures and holding times.

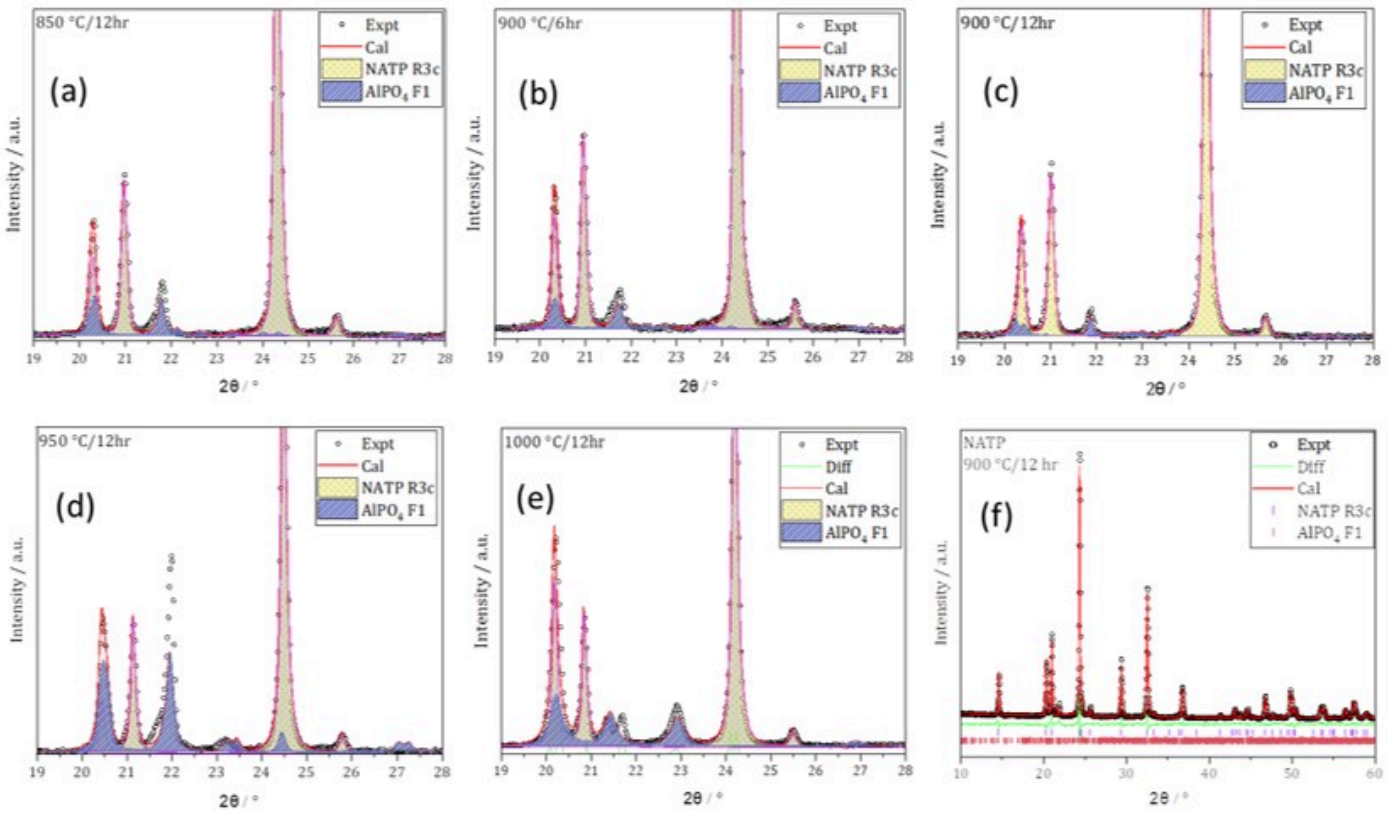

Figure 6

Zoom-in plots of the full pattern Rietveld refinement of $Na_{1.3}Al_{0.3}Ti_{1.7}(PO_4)_3$ with the (blue) peaks representing the composition of the $AlPO_4$ impurity phase and (yellow) peaks representing NATP (a) 850 °C/12 hr, (b) (b) 900 °C/6 hr, (c) (c) 900 °C/12 hr, (d) (d) 950 °C/12 hr, (e) 1000 °C/12 hr, (f) Full pattern Rietveld refinement of NATP sintered at 900 °C/12 hr.

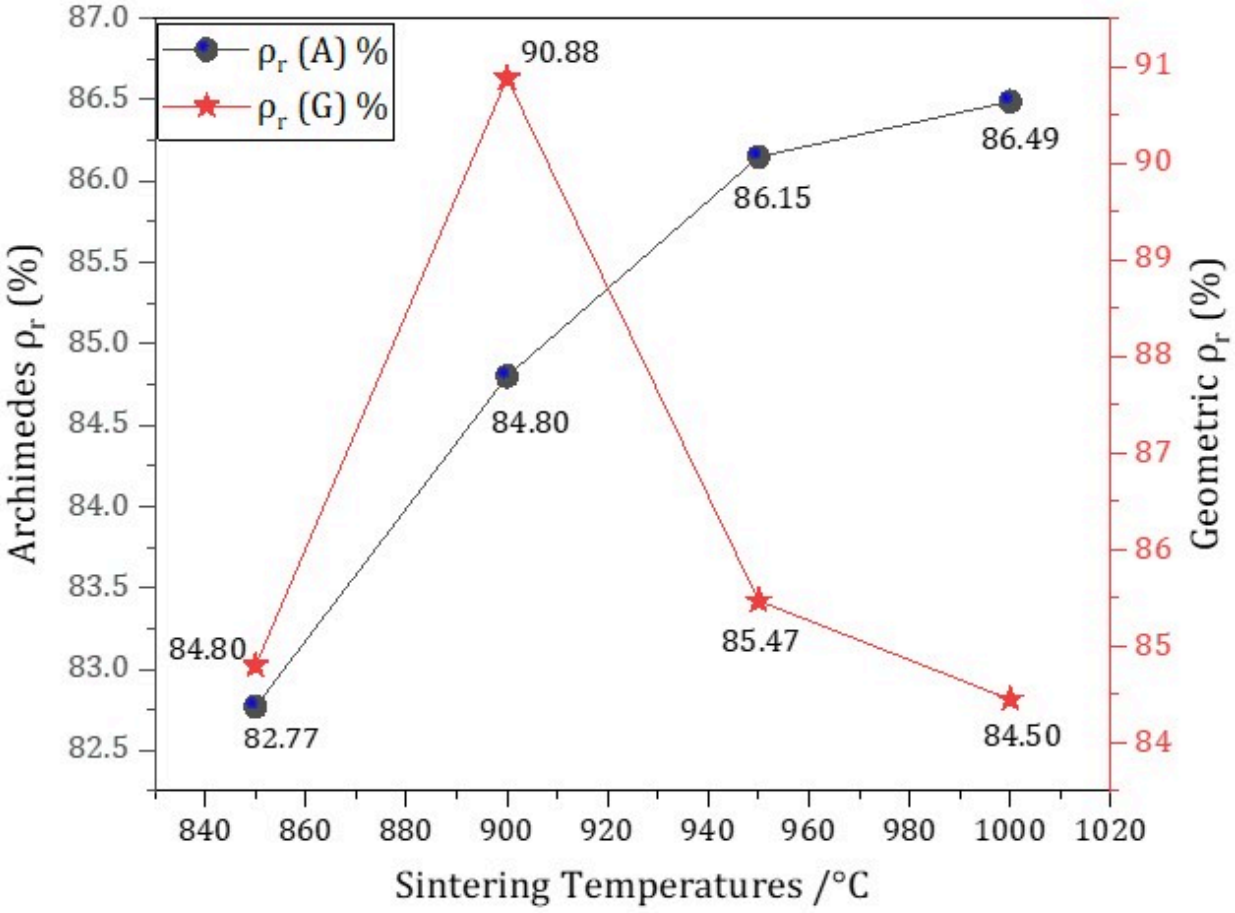

Figure 7

Relative density of $Na_{1.3}Al_{0.3}Ti_{1.7}PO_{12}$ at different sintering temperatures for 12 hr using Archimedes and geometric methods.

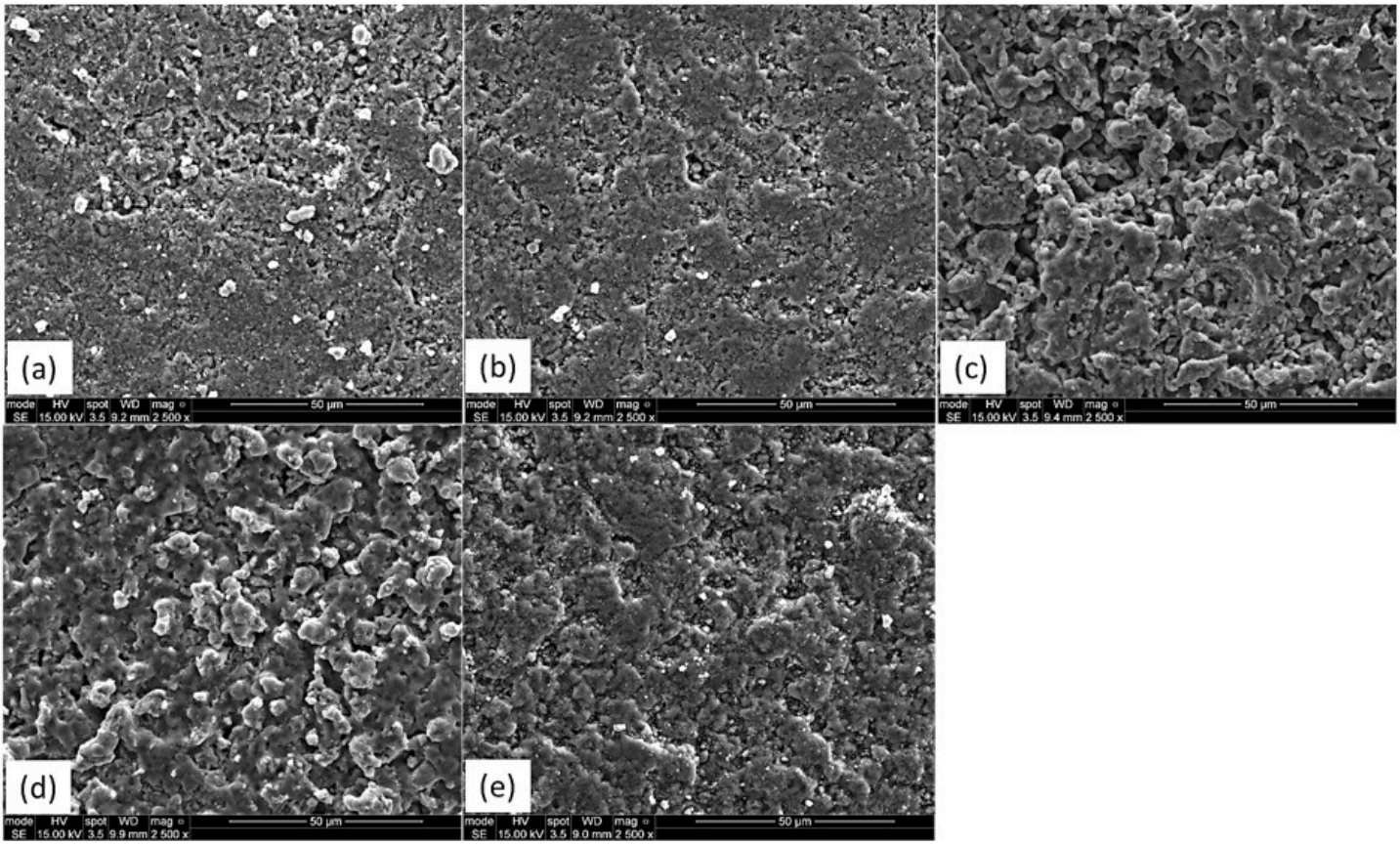

Figure 8

SEM micrographs of NATP surfaces (a) 850 °C/12 hr, (b) 900 °C/6 hr, (c) 900 °C/12 hr, (d) 950 °C/12 hr and (e) 1000 °C/12 hr.

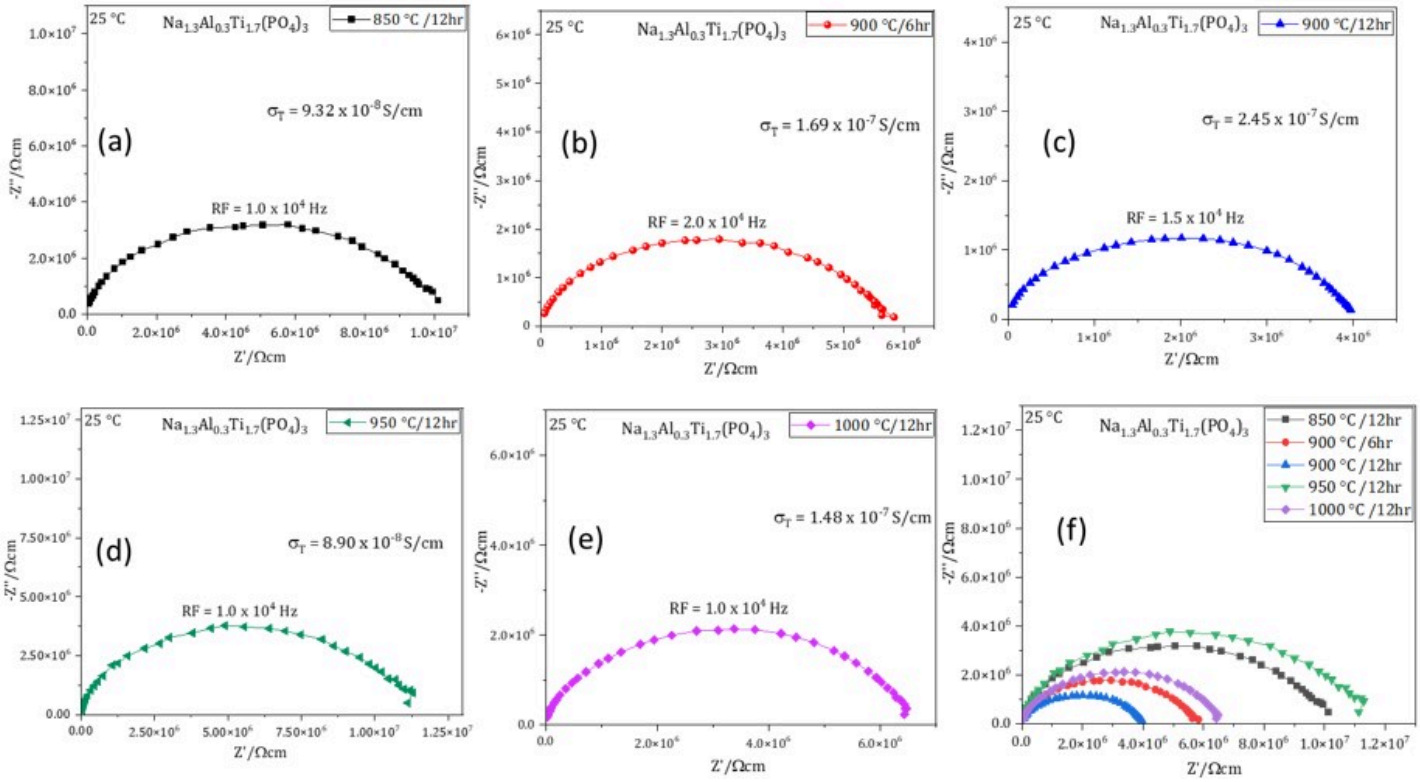

Figure 9

Complex impedance plots of $Na_{1.3}Al_{0.3}Ti_{1.7}PO_{12}$ at 25 °C (a) 850 °C/12 hr, (b) 900 °C/6 hr, (c) 900 °C/12 hr, (d) 950 °C/12 hr, (e) 1000 °C/12 hr, (f) at different temperatures and times.

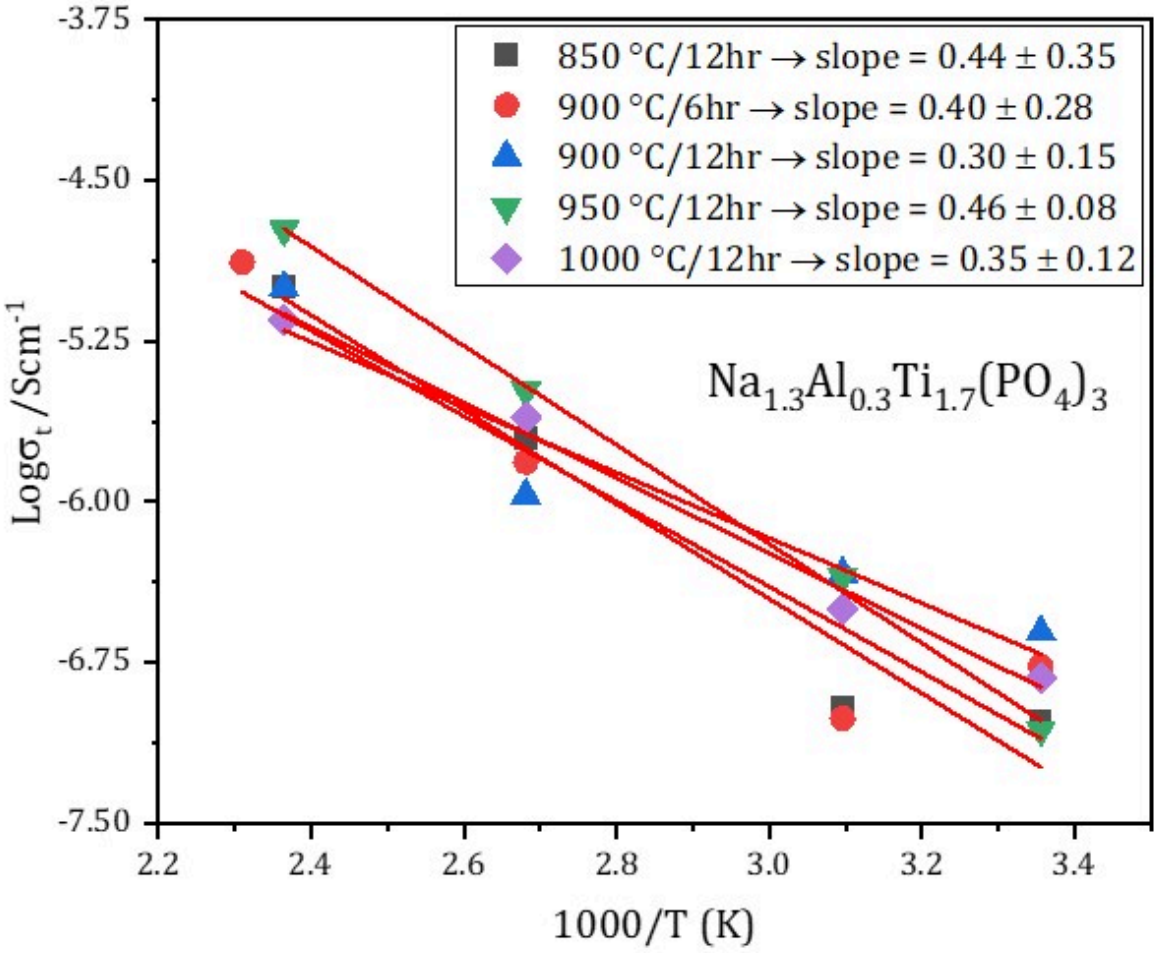

Figure 10

Arrhenius plots of the total conductivity for NATP ceramics at different sintering temperatures.

Supplementary Files

This is a list of supplementary files associated with this preprint. Click to download.

- SupportingInformationNATP.docx